ACSNANO

www.acsnano.org

ARTICLE

High-Quality Hexagonal Boron Nitride from 2D Distillation

Huanyao Cun,*,§ Zichun Miao,§ Adrian Hemmi, Yasmine Al-Hamdani, Marcella Iannuzzi, Jürg Osterwalder, Michael S. Altman, and Thomas Greber

Cite This: https://dx.doi.org/10.1021/acsnano.0c08616

ABSTRACT: The production of high-quality two-dimensional (2D) materials is essential for the ultimate performance of single layers and their hybrids. Hexagonal boron nitride (*h*-BN) is foreseen to become the key 2D hybrid and packaging material since it is insulating, impermeable, flat, transparent, and chemically inert, though it is difficult to attain in ultimate quality. Here, a scheme is reported for producing single layer *h*-BN that shows higher quality in view of mosaicity and strain variations than material from chemical vapor deposition (CVD). We delaminate CVD *h*-BN from Rh(111) and transfer it to a clean metal surface. The twisting angle between BN and the second substrate yields metastable moiré structures. Annealing above 1000 K leads to 2D distillation, *i.e.*, catalyst-assisted BN sublimation from the edges of the transferred layer and subsequent condensation into superior quality *h*-BN. This provides a way for 2D material production remote from CVD instrumentation.

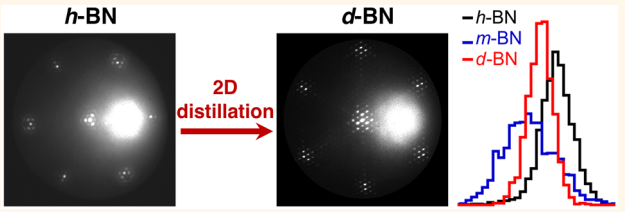

KEYWORDS: *h-BN, 2D materials transfer, moiré, heterogeneous catalysis, 2D distillation*

INTRODUCTION

The paradigm "two-dimensional (2D) materials"[1] is expected to enable opportunities for devices with ultimately thin membranes,[2] mechanical detectors,[3] inks,[4] and specifically for electronics beyond silicon technology.[5,6] These materials can be assembled at room temperature, layer by layer, which allows us to produce nonequilibrium hybrid structures. For instance, the twisting of two stacked graphene layers leads to 2D superconductivity that is related to the moiré interference between the two 2D lattices.[7]

Before harvesting the benefits of materials, their fabrication and handling have to be mastered. This is a big challenge for 2D materials since they mostly consist of surfaces that are known to be prone to imperfections like contaminations and defects. The related reactivity of 2D materials calls for a packaging material that is protective, impermeable, thin, flat, transparent, and nonreactive. Hexagonal boron nitride (*h*-BN) has all these properties and is the prime candidate to become the key 2D packaging and hybrid material.[8] Currently, the main approach for scalable production is chemical vapor deposition (CVD) of precursors that contain boron and nitrogen[9−14] and segregation-assisted growth[15,16] on substrates acting as catalysts or bulk reservoirs of B and N.[17] Although CVD does not allow the preparation of single orientation *h*-BN on all substrates, transfer of single-orientation *h*-BN does, with the added feature of nonequilibrium moiré formation with arbitrary lattice orientation. However, transfer is another challenge, since it is, if successful, often accompanied by compromises to the material quality.[18,19]

In view of these problems and opportunities, we transferred CVD-grown single layer boron nitride back onto a crystalline catalyst. The introduction of a twist angle enables moiré interference between the second substrate and the *h*-BN layer. Annealing of such structures reveals the temperature window, within which this moiré structure is efficiently cleaned and stable. At higher temperatures this metastable moiré undergoes a phase transformation where boron nitride sublimates from the edge of the transferred BN into a dilute adsorbate phase and a recondensation into a lattice aligned higher quality *h*-BN. Because the sublimation and recondensation processes are well confined to the substrate surface, we label it "2D distillation". This is a way to produce *h*-BN from transferred material with holes and contaminations and remote from CVD equipment. All these products and processes can be directly monitored in real time with low energy electron microscopy (LEEM).

Single orientation *h*-BN monolayers on rhodium, also called "nanomesh",[10,20] are fabricated in a CVD process on single

Received: October 15, 2020
Accepted: December 16, 2020

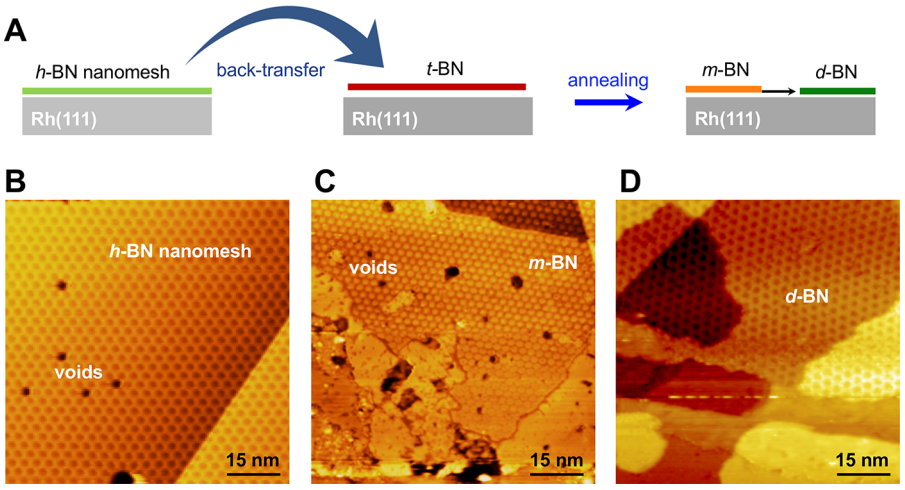

Figure 1. Transfer and annealing of *h*-BN on Rh(111). (A) Concept: After growth and delamination, the *h*-BN monolayer is transferred on a Rh(111) substrate, where *t*-BN forms. Annealing of *t*-BN leads to visible moiré structures (*m*-BN), and at higher temperature *m*-BN distills into *d*-BN; *i.e.*, nanomesh reforms; (B-D) Room temperature STM (80 × 80 nm^2) images of pristine *h*-BN nanomesh with 2 nm voids on Rh(111) (B), *m*-BN with voids on Rh(111) after transfer and annealing to 750 K (C), and distilled *m*-BN without voids on Rh(111) (*d*-BN) after transferred and annealing above 1000 K (D). $U = -1.20$ V, $I = 0.50$ nA.

crystalline Rh(111) at a 4-in. wafer scale.[21] As on Ru(0001),[22] the interaction of BN with the substrate is relatively strong and aligned *h*-BN can be grown while, *e.g.*, no pronounced azimuthal lock-in was observed for Pd(111).[23]

RESULTS AND DISCUSSION

Figure 1A depicts the procedure of the experiments. After CVD growth, a *h*-BN monolayer was transferred (named *t*-BN) on arbitrary substrates.[18,19] Here, we investigate the transfer of *h*-BN onto Rh(111). X-ray photoelectron spectroscopy (XPS) data in Figure S1 of the Supporting Information (SI) confirms successful transfer of *h*-BN layer. Notably the lattices of *t*-BN and the Rh substrate are not aligned, as is the case for the *h*-BN nanomesh. Annealing to 750 K cleans the surface, which induces the formation of moiré structures (*m*-BN) that can be resolved with scanning tunneling microscopy (STM). The *m*-BN is metastable, and annealing to higher temperatures leads to a more stable phase (*d*-BN): the process that we call "2D distillation". The process is robust and was observed for all *m*-BN moiré structures with twist angles between 4 and 25° that were investigated. Figure 1B shows a STM image of a CVD-grown *h*-BN nanomesh on Rh(111).[10] Prior to the imaging, 2 nm voids have been created with the "can-opener" effect[24,25] in order to have the fingerprint of the original BN layer after transfer.[18] Figure 1C displays a representative STM image of *m*-BN with such 2 nm voids. Clearly, a hexagonal superlattice is distinguished. Compared to the nanomesh in Figure 1B, the moiré lattice constant is 25% smaller, and the unit cell displays a 0.1 nm protrusion and not a depression (more data can be found in Figure S2 of the SI). Applying the theory for a periodic overlayer moiré pattern,[26] the superlattice constant of 2.4 nm indicates that this transferred *t*-BN flake was rotated by $\alpha = 4°$ with respect to the Rh lattice. Figure 1D shows a region of the surface after further annealing to above 1000 K. The formation of a superstructure with a lattice constant of 3.2 nm, which is within the error bar of the *h*-BN nanomesh, is observed. Furthermore, the 2 nm voids as seen in Figure 1B,C disappeared.

For the study of macro- and mesoscopic properties of transferred BN at the millimeter scale, other methods than STM have to be employed. While low energy electron diffraction (LEED) maps the macroscopic crystallinity, ultraviolet photoelectron spectroscopy (UPS) provides details on the electronic structures. An *m*-BN sample with a lattice rotation angle $\alpha = 19°$ and a transfer rate of 95% is compared with a nanomesh ($\alpha = 0°$) in Figure 2. The moiré is formed after transfer and annealing to 750 K. The angle α between the $[1\bar{1}0]$ direction of the substrate and the [10] direction of the adsorbate is determined from the LEED patterns in Figure 2A,B. Normal emission angle-resolved photoemission spectroscopy (ARPES) displays a σ band splitting $\Delta_{\alpha'\beta'}$ of 0.6 eV for this *m*-BN and an upshift $\Delta_{\alpha\alpha'}$ of the σ_α bands by 0.27 eV to 4.27 eV binding energy. This upshift is in line with the *h*-BN physisorption picture,[9] which indicates for the present case that the work function of the $\alpha = 19°$ moiré is 0.2 eV higher than that of the *h*-BN nanomesh. The σ_α and σ_β band-positions are measures for the electrostatic potential variations in the boron nitride supercell, and it can be seen that this splitting decreases by about a factor of 2 from the nanomesh to the $\alpha = 19°$ moiré. The fact that the supercell lattice constant decreases by a factor of 4.24 implies even larger lateral electric fields than in the *h*-BN nanomesh.[27] The interpretation of the photoemission results is supported by density functional theory (DFT) with the calculation of 19 *h*-BN units rotated by an angle of 23.4° on top of a (4 × 4) Rh unit cell. It predicts that the bonding of the rotated *h*-BN layer with the substrate is about 20% weaker than the aligned 169 on 144 R0° *h*-BN/Rh(111) nanomesh (see S4.1 in the SI).[28]

The properties of 2D materials strongly depend on their lattice: strain fluctuations and lattice rotation angle distributions at the micrometer scale are decisive. For the case of graphene lattice, strain may be measured with Raman spectroscopy.[29,30] If it comes to a noninvasive method that captures the lattice rotation and the related moiré angles on the mesoscopic scale, LEEM gives direct insight.[31−36] LEEM identifies different phases in bright field images, where the specular electron reflectivity is measured, while the local crystal lattice orientation and straining can be inferred from μ-LEED

https://dx.doi.org/10.1021/acsnano.0c08616
ACS Nano XXXX, XXX, XXX−XXX

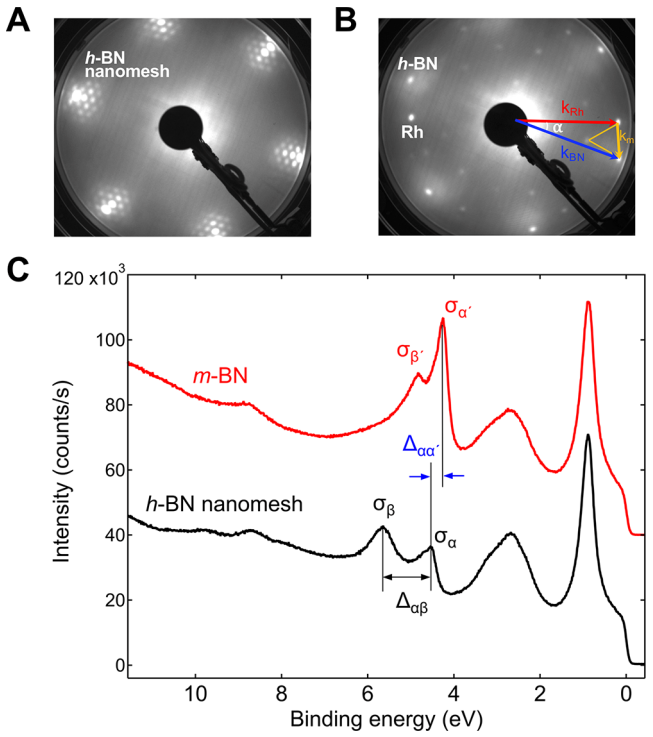

Figure 2. Structural and electronic properties of *h*-BN/Rh(111) and *m*-BN/Rh(111). (A, B) LEED patterns (E = 70 eV) of pristine *h*-BN nanomesh (A), and transferred *h*-BN on Rh(111) after annealing to 750 K (*m*-BN) (B). The reciprocal lattice vectors of Rh(111), *h*-BN, and the superstructures are indicated. The angle α between the substrate $\vec{k}_{Rh}$ (red) and *h*-BN ⟨10⟩ diffraction spots $\vec{k}_{BN}$ (blue) is 19°. $\vec{k}_{BN}-\vec{k}_{Rh}$ is the reciprocal moiré lattice vector $\vec{k}_m$ (orange). (C) UPS (He I_α) spectra of pristine *h*-BN nanomesh (black) and *m*-BN (red) in (B). The work function increase of *m*-BN/Rh(111) is reflected in the σ band shift $\Delta_{\alpha\alpha'}$. The σ-band splitting $\Delta_{\alpha\beta}$ is smaller in *m*-BN.

diffraction patterns measured on 250 nm length scale.[36] Furthermore, LEEM can be performed at high temperatures, which allows us to directly observe phase transformations from *t*-BN into *d*-BN in real space and time.

Figure 3 shows LEEM data from a single layer *h*-BN with 2 nm voids that was transferred on a Rh(111) thin film substrate and annealed to different temperatures. Figure 3A discerns *t*-BN and *m*-BN phases within the field-of-view of 23 μm at 1130 K. The transformation reaction starts at catalytic particle sites (condensation seed, see S5.2 and Figure S7 in the SI). The zoom-in area (yellow dashed circle in Figure 3A,F) in Figure 3B−E document the 2D distillation process of *m*-BN to *d*-BN and show that the reaction proceeds with speeds in the order of 10 nm/s without the presence of BN precursor molecules in the gas phase and with less than 50% loss of BN (see the LEEM movie and analysis details in S5.1 of the SI). Since boron binds more strongly to Rh(111) than nitrogen does (see section 4.2 of the SI), a supply of nitrogen from the gas phase could decrease the loss of BN due to N desorption during distillation. This is also a hint that the observed $(2\sqrt{3} \times 2\sqrt{3})$R30° superstructure on the bare rhodium near *d*-BN (see Figure S8 in the SI) is a boron-induced reconstruction. The distillation occurred on a tens of micron length scale at numerous independent locations on the sample, limited by the annealing time. In Figure 3F, the *d*-BN structure dominates, where straight segments at the edges of the *d*-BN patches

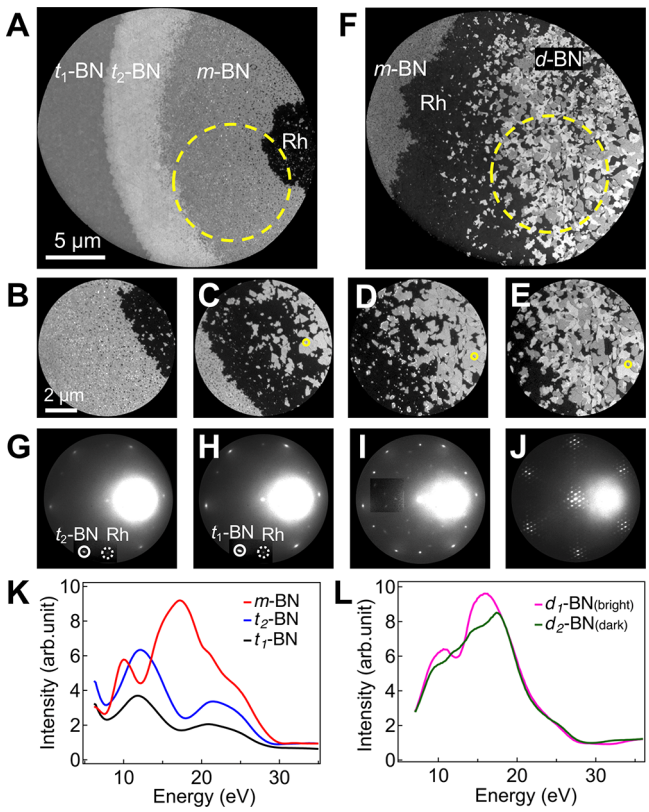

Figure 3. Low electron energy microscopy (LEEM) images, patterns and spectra. (A−F) LEEM bright-field image sequence of the transformation from *t*-BN to *m*-BN, and 2D distillation to *d*-BN upon annealing (see LEEM video in the SI). The yellow circle in C−E is a marker at the same location on the sample to guide the viewers for how the *d*-BN evolves: (A) 1130 K, t = 0; (B) 1135 K, t = 11 min; (C) 1180 K, t = 19 min; (D) 1180 K, t = 28 min; (E) 1210 K, t = 38 min; (F) 1210 K, t = 47 min. (B−E) Zoom-ins of the area indicated by the yellow dashed-circles in (A) and (F). The imaging energies are 12 eV in (A)−(D) and 15 eV in (E) and (F). The μ-LEED patterns of (G) t_2-BN, (H) t_1-BN, (I) *m*-BN, and (J) *d*-BN were recorded at room temperature after annealing to 1100 K (G−I) and 1210 K (J). t_2-BN, t_1-BN, and Rh spots are highlighted by white solid-line and dashed-line circles in (G) and (H). (K, L) LEEM I(V) spectra of different phases are measured after recording the corresponding μ-LEED patterns. (K) t_1-BN (black), t_2-BN (blue), and *m*-BN (red). (L) *d*-BN twin domains of d_1 (magenta) and d_2 (green).

reveal the crystallographic orientation of the *d*-BN. Furthermore, *d*-BN exhibits two intensities in Figure 3F that identify BN/substrate twinning domains. The structural natures of the different crystalline phases are distinguished by the μ-LEED patterns in Figure 3G−J obtained from 250 nm diameter areas. The rotated *t*-BN layer shows Rh and rotated BN integer diffraction spots only. In the *m*-BN phase, the diffraction spots of the moiré lattice are visible and from the lower photoelectron yield of *m*-BN we infer a lower work function of *t*-BN (for details, see section S5.2 in the SI). Finally, the diffraction pattern of *d*-BN is reminiscent of *h*-BN/Rh(111) nanomesh with a commensurate 13 × 13 on 12 × 12 superstructure. The variation of the elastically scattered intensity along the surface normal versus incident electron energy in I(V) spectra gives rise to the energy dependence of bright field LEEM image contrast and also distinguishes various phases. The I(V) spectra of t_1-BN and t_2-BN in Figure

https://dx.doi.org/10.1021/acsnano.0c08616
ACS Nano XXXX, XXX, XXX−XXX

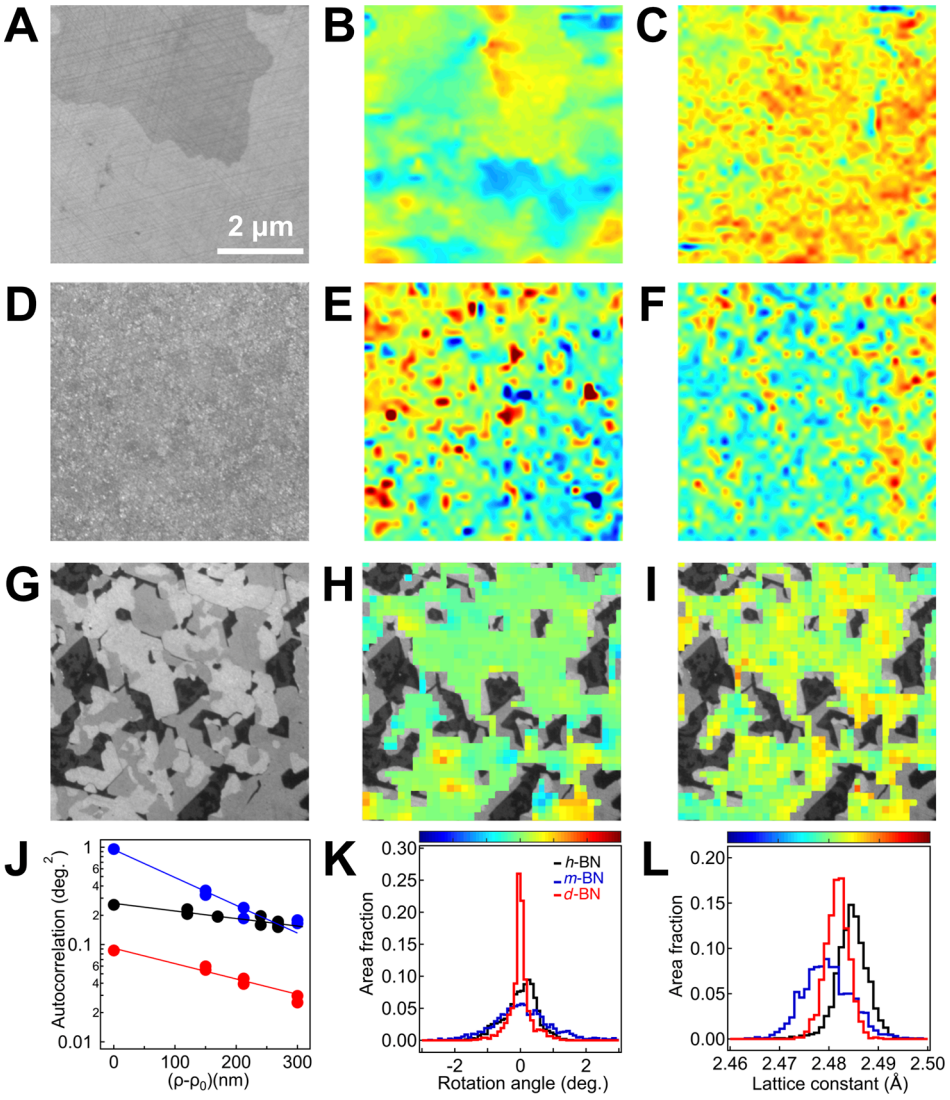

Figure 4. BN lattice properties from scanning μ-LEED at room temperature. (A–C) *h*-BN nanomesh grown on Rh(111) and annealed to 1210 K. (D–F) *m*-BN after annealing to 1100 K. (G–I) *d*-BN distilled from *m*-BN up to 1210 K. (A, D, G) LEEM bright field images. Color-coded (B, E, H) lattice rotation angles, α, and (C, F, I) lattice constants. (J–L) Characteristics of *h*-BN (black), *m*-BN (blue), and *d*-BN (red). (J) Spatial autocorrelation of lattice rotation angles. (K) Histogram of the lattice rotation angles. The average *m*-BN rotation angle of 24.3° is subtracted. (L) Histogram of the lattice constants.

3A are displayed in Figure 3K and show similar characteristics, while *m*-BN is distinctly different. The similarity of the I(V) spectra for t_1-BN and t_2-BN indicate that they have the same structure, but the higher intensity of t_2-BN means that it is cleaner. This cleaning process precedes the 2D distillation (see the video in the SI). Figure 3L displays the I(V) spectra for two different BN domains d_1-BN and d_2-BN in Figure 3F.

The *in situ* LEEM observations directly reveal the 2D distillation process, *i.e.*, the sublimation of BN onto the Rh(111) surface, the diffusion of these precursors, and condensation into a more stable material: *d*-BN. The residence-times of B and N on the surface are sufficiently long for this process to take place. Free *h*-BN fragments continue to be generated at the receding *m*-BN edge and diffuse toward the *d*-BN phase in response to the free energy difference between the *m*-BN and *d*-BN edges, respectively. This picture should be generally valid and applicable to the distillation growth of other 2D materials on Rh and other catalytic material surfaces used for CVD growth and transfer.

The *m*-BN → *d*-BN phase transformation is initiated at sparsely distributed defect sites (Figure S7). These defects are believed to be Rh particles bound to the underside of the transferred *h*-BN that were detached from the growth substrate during the transfer process. The areal density of the particles is in the order of 10^{-4} μm^{-2}. These point defects trigger the 2D distillation at low temperature, which is favorable for minimizing the loss of BN from the surface[19] and explain the circular shape of the phase transformation region. The choice of the catalyst surface plays an important role, as there is no evidence for 2D distillation in control experiments with *h*-BN on a SiO_2 surface (Figure S3).

In order to establish differences in the quality of *h*-BN nanomesh, *m*-BN and *d*-BN, lattice constants, lattice rotation angles, and mosaicities were determined quantitatively in submicron (250 nm) areas with high accuracy using μ-LEED. These characteristics are particularly relevant for the electronic performance of 2D materials. Figure 4 shows 6 × 6 μm^2 scanning μ-LEED images of a *h*-BN nanomesh, *m*-BN and *d*-

https://dx.doi.org/10.1021/acsnano.0c08616
ACS Nano XXXX, XXX, XXX–XXX

BN. As for *d*-BN, *h*-BN may display in different domains as well, which explains the bright field contrast in Figure 4A, while such contrast is absent in the shown *m*-BN patch. The BN lattice rotation angles α and lattice constants *a* have been determined from more than 1000 different μ-LEED patterns recorded in the scan areas. The BN lattice constants of *d*-BN have the smallest scatter of 0.1%, while for *m*-BN it is about a factor of 2 larger. The average BN lattice rotation angle of *m*-BN is 24.3°, while *h*-BN and *d*-BN appear aligned to the Rh substrate. The mosaic spread or standard deviation of these angles is the smallest for *d*-BN. This is also reflected in the prefactors of the lateral autocorrelation of the rotation angles and we find the best correlation length λ_α of 560 nm for *h*-BN nanomesh, while it is 280 nm for *d*-BN and 150 nm for *m*-BN (see detailed analysis in S5.5 in the SI).

CONCLUSIONS

In summary, 2D distillation signifies gas-phase and precipitation induced growth as a way to synthesize 2D materials on surfaces. We investigated hexagonal boron nitride that is transferred back onto a rhodium substrate. Annealing of an arbitrarily oriented transferred single layer cleans the BN layer and leads to moiré interference with the substrate. Further annealing treatments lead to formation of *d*-BN by sublimation and recondensation with distinctly superior quality compared with the initially grown *h*-BN. Our results provide a method for fabricating high-quality *h*-BN monolayers without CVD setup. 2D distillation promises a synthesis route for any 2D material on catalytic substrates.

MATERIALS AND METHODS

CVD, Delamination, XPS, UPS, LEED, STM, and Raman Experiments. The *h*-BN monolayers are prepared with an ultrahigh vacuum (UHV) CVD method on 4-in. single-crystalline Rh(111) thin film wafers with a base pressure of 1×10^{-10} mbar.[37] For the 2 nm void generation with the "can-opener" effect, a Specs IQP 10/35 Penning-type ion source run at lowest acceleration potential was used.[24] The electrochemical delamination procedure of *h*-BN monolayer is described in detail in refs 18 and 19. XPS and UPS measurements were carried out in a VGESCALAB 220 system.[38] The STM experiments were performed in a variable-temperature scanning tunneling microscope (Omicron, VT-STM).[39]

LEEM Experiments. LEEM imaging and I(V) spectra measurements, conventional and scanning μ-LEED and PEEM were carried out in a noncommercial LEEM instrument.[36,40−42] PEEM measurements were performed using illumination from a mercury discharge lamp. Temperature was measured using an optical pyrometer with an emissivity setting of 0.1.

DFT Simulations. DFT simulations have been performed with the CP2K code[43] using the PBE-rVV10 density functional.[44−46] The ground-state calculations have been carried out under the Gaussian plane wave method and the molecular orbitals of the valence electrons are expanded into a combination of Gaussian and plane waves, whereas the core electrons are treated using Goedecker−Teter−Hutter pseudopotentials.[47] For the Gaussian basis set expansion, the valence orbitals have been expanded into molecularly optimized DZVP basis sets for all elements except Rh, where orbitals were expanded using a molecularly optimized SZVP basis.[48]

ASSOCIATED CONTENT

Supporting Information

The Supporting Information is available free of charge at https://pubs.acs.org/doi/10.1021/acsnano.0c08616.

XPS of back-transferred *h*-BN on Rh(111), STM of other moiré patterns, XPS and Raman analysis of back-transferred *h*-BN on SiO_2, DFT calculations, LEEM, PEEM and μ-LEED evaluations, including LEEM movie analysis, condensation seed, the $(2\sqrt{3} \times 2\sqrt{3})R30°$ superstructure, recording sites of μ-LEED and I(V) curves, and detailed μ-LEED evaluations (PDF)

LEEM movie (MP4)

AUTHOR INFORMATION

Corresponding Author

Huanyao Cun − *Physik-Institut, Universität Zürich, 8057 Zürich, Switzerland;* orcid.org/0000-0002-5225-9861; Email: hycun1@physik.uzh.ch

Authors

Zichun Miao − *Department of Physics, Hong Kong University of Science and Technology, Kowloon, Hong Kong SAR, China*

Adrian Hemmi − *Physik-Institut, Universität Zürich, 8057 Zürich, Switzerland*

Yasmine Al-Hamdani − *Department of Chemistry, University of Zürich, 8057 Zürich, Switzerland*

Marcella Iannuzzi − *Department of Chemistry, University of Zürich, 8057 Zürich, Switzerland;* orcid.org/0000-0001-9717-2527

Jürg Osterwalder − *Physik-Institut, Universität Zürich, 8057 Zürich, Switzerland;* orcid.org/0000-0001-9517-641X

Michael S. Altman − *Department of Physics, Hong Kong University of Science and Technology, Kowloon, Hong Kong SAR, China*

Thomas Greber − *Physik-Institut, Universität Zürich, 8057 Zürich, Switzerland;* orcid.org/0000-0002-5234-1937

Complete contact information is available at: https://pubs.acs.org/10.1021/acsnano.0c08616

Author Contributions

[§]H.C. and Z.M. contributed equally to this work.

Notes

The authors declare no competing financial interest.

ACKNOWLEDGMENTS

Financial support by the European Commission under the Graphene Flagship Core 2 (No. 785219) and the HKUST Block Grant DSCI17SC02 are gratefully acknowledged. We thank Mr. Michael Weinl and Dr. Matthias Schreck from Universität Augsburg, Germany for providing Rh metal substrates.

REFERENCES

(1) Geim, A. K.; Grigorieva, I. V. van der Waals Heterostructures. *Nature* **2013**, *499*, 419−425.

(2) Surwade, S. P.; Smirnov, S. N.; Vlassiouk, I. V.; Unocic, R. R.; Veith, G. M.; Dai, S.; Mahurin, S. M. Water Desalination Using Nanoporous Single-Layer Graphene. *Nat. Nanotechnol.* **2015**, *10*, 459−464.

(3) Cartamil-Bueno, S. J.; Cavalieri, M.; Wang, R.; Houri, S.; Hofmann, S.; van der Zant, H. S. J. Mechanical Characterization and Cleaning of CVD Single-Layer h-BN Resonators. *NPJ. 2D Mater. Appl.* **2017**, *1*, 1−7.

(4) Torrisi, F.; Hasan, T.; Wu, W.; Sun, Z.; Lombardo, A.; Kulmala, T. S.; Hsieh, G.-W.; Jung, S.; Bonaccorso, F.; Paul, P. J.; Chu, D.; Ferrari, A. C. Inkjet-Printed Graphene Electronics. *ACS Nano* **2012**, *6*, 2992−3006.

https://dx.doi.org/10.1021/acsnano.0c08616
ACS Nano XXXX, XXX, XXX−XXX

(5) Novoselov, K. S.; Geim, A. K.; Morozov, S. V.; Jiang, D.; Zhang, Y.; Dubonos, S. V.; Grigorieva, I. V.; Firsov, A. A. Electric Field Effect in Atomically Thin Carbon Films. *Science* **2004**, *306*, 666−669.
(6) Banszerus, L.; Schmitz, M.; Engels, S.; Dauber, J.; Oellers, M.; Haupt, F.; Watanabe, K.; Taniguchi, T.; Beschoten, B.; Stampfer, C. Ultrahigh-Mobility Graphene Devices from Chemical Vapor Deposition on Reusable Copper. *Sci. Adv.* **2015**, *1*, No. e1500222.
(7) Cao, Y.; Fatemi, V.; Fang, S.; Watanabe, K.; Taniguchi, T.; Kaxiras, E.; Jarillo-Herrero, P. Unconventional Superconductivity in Magic-Angle Graphene Superlattices. *Nature* **2018**, *556*, 43−50.
(8) Dean, C. R.; Young, A. F.; Meric, I.; Lee, C.; Wang, L.; Sorgenfrei, S.; Watanabe, K.; Taniguchi, T.; Kim, P.; Shepard, K. L.; Hone, J. Boron Nitride Substrates for High-Quality Graphene Electronics. *Nat. Nanotechnol.* **2010**, *5*, 722−726.
(9) Nagashima, A.; Tejima, N.; Gamou, Y.; Kawai, T.; Oshima, C. Electronic Structure of Monolayer Hexagonal Boron Nitride Physisorbed on Metal Surfaces. *Phys. Rev. Lett.* **1995**, *75*, 3918−3921.
(10) Corso, M.; Auwärter, W.; Muntwiler, M.; Tamai, A.; Greber, T.; Osterwalder, J. Boron Nitride Nanomesh. *Science* **2004**, *303*, 217−220.
(11) Farwick zum Hagen, F. H.; Zimmermann, D. M.; Silva, C. C.; Schlueter, C.; Atodiresei, N.; Jolie, W.; Martínez-Galera, A. J.; Dombrowski, D.; Schröder, U. A.; Will, M.; Lazić, P.; Caciuc, V.; Blügel, S.; Lee, T.-L.; Michely, T.; Busse, C. Structure and Growth of Hexagonal Boron Nitride on Ir(111). *ACS Nano* **2016**, *10*, 11012−11026.
(12) Lee, J. S.; Choi, S. H.; Yun, S. J.; Kim, Y. I.; Boandoh, S.; Park, J.-H.; Shin, B. G.; Ko, H.; Lee, S. H.; Kim, Y.-M.; Lee, Y. H.; Kim, K. K.; Kim, S. M. Wafer-Scale Single-Crystal Hexagonal Boron Nitride Film *via* Self-Collimated Grain Formation. *Science* **2018**, *362*, 817−821.
(13) Wang, L.; Xu, X.; Zhang, L.; Qiao, R.; Wu, M.; Wang, Z.; Zhang, S.; Liang, J.; Zhang, Z.; Zhang, Z.; Chen, W.; Xie, X.; Zong, J.; Shan, Y.; Guo, Y.; Willinger, M.; Wu, H.; Li, Q.; Wang, W.; Gao, P.; et al. Epitaxial Growth of a 100-Square-Centimetre Single-Crystal Hexagonal Boron Nitride Monolayer on Copper. *Nature* **2019**, *570*, 91−95.
(14) Chen, T.-A.; Chuu, C.-P.; Tseng, C.-C.; Wen, C.-K.; Wong, H. S. P.; Pan, S.; Li, R.; Chao, T.-A.; Chueh, W.-C.; Zhang, Y.; Fu, Q.; Yakobson, B. I.; Chang, W.-H.; Li, L.-J. Wafer-Scale Single-Crystal Hexagonal Boron Nitride Monolayers on Cu(111). *Nature* **2020**, *579*, 219−223.
(15) Suzuki, S.; Pallares, R. M.; Hibino, H. Growth of Atomically Thin Hexagonal Boron Nitride Films by Diffusion through a Metal Film and Precipitation. *J. Phys. D: Appl. Phys.* **2012**, *45*, 385304.
(16) Zhang, C.; Fu, L.; Zhao, S.; Zhou, Y.; Peng, H.; Liu, Z. Controllable Co-Segregation Synthesis of Wafer-Scale Hexagonal Boron Nitride Thin Films. *Adv. Mater.* **2014**, *26*, 1776−1781.
(17) Auwaerter, W. Hexagonal Boron Nitride Monolayers on Metal Supports: Versatile Templates for Atoms, Molecules and Nanostructures. *Surf. Sci. Rep.* **2019**, *74*, 1−95.
(18) Cun, H. Y.; Hemmi, A.; Miniussi, E.; Bernard, C.; Probst, B.; Liu, K.; Alexander, D. T. L.; Kleibert, A.; Mette, G.; Weinl, M.; Schreck, M.; Osterwalder, J.; Radenovic, A.; Greber, T. Centimeter-Sized Single-Orientation Monolayer Hexagonal Boron Nitride with or without Nanovoids. *Nano Lett.* **2018**, *18*, 1205−1212.
(19) Hemmi, A.; Cun, H. Y.; Tocci, G.; Epprecht, A.; Stel, B.; Lingenfelder, M.; de Lima, L. H.; Muntwiler, M.; Osterwalder, J.; Iannuzzi, M.; Greber, T. Catalyst Proximity-Induced Functionalization of h-BN with Quat Derivatives. *Nano Lett.* **2019**, *19*, 5998−6004.
(20) Berner, S.; Corso, M.; Widmer, R.; Groening, O.; Laskowski, R.; Blaha, P.; Schwarz, K.; Goriachko, A.; Over, H.; Gsell, S.; Schreck, M.; Sachdev, H.; Greber, T.; Osterwalder, J. Boron Nitride Nanomesh: Functionality from a Corrugated Monolayer. *Angew. Chem., Int. Ed.* **2007**, *46*, 5115−5119.
(21) Gsell, S.; Fischer, M.; Schreck, M.; Stritzker, B. Epitaxial Films of Metals from the Platinum Group (Ir, Rh, Pt and Ru) on YSZ-Buffered Si(111). *J. Cryst. Growth* **2009**, *311*, 3731−3736.
(22) Goriachko, A.; He; Knapp, M.; Over, H.; Corso, M.; Brugger, T.; Berner, S.; Osterwalder, J.; Greber, T. Self-Assembly of a Hexagonal Boron Nitride Nanomesh on Ru(0001). *Langmuir* **2007**, *23*, 2928−2931.
(23) Morscher, M.; Osterwalder, J.; Greber, T. Formation of Single Layer h-BN on Pd(111). *Surf. Sci.* **2006**, *600*, 3280−3284.
(24) Cun, H. Y.; Iannuzzi, M.; Hemmi, A.; Roth, S.; Osterwalder, J.; Greber, T. Immobilizing Individual Atoms beneath a Corrugated Single Layer of Boron Nitride. *Nano Lett.* **2013**, *13*, 2098−2103.
(25) Cun, H. Y.; Iannuzzi, M.; Hemmi, A.; Osterwalder, J.; Greber, T. Two-Nanometer Voids in Single-Layer Hexagonal Boron Nitride: Formation *via* the "Can-Opener" Effect and Annihilation by Self-Healing. *ACS Nano* **2014**, *8*, 7423−7431.
(26) Hermann, K. Periodic Overlayers and Moire Patterns: Theoretical Studies of Geometric Properties. *J. Phys.: Condens. Matter* **2012**, *24*, 314210.
(27) Dil, H.; Lobo-Checa, J.; Laskowski, R.; Blaha, P.; Berner, S.; Osterwalder, J.; Greber, T. Surface Trapping of Atoms and Molecules with Dipole Rings. *Science* **2008**, *319*, 1824−1826.
(28) Iannuzzi, M.; Tran, F.; Widmer, R.; Dienel, T.; Radican, K.; Ding, Y.; Hutter, J.; Gröning, O. Site-Selective Adsorption of Phthalocyanine on h-BN/Rh(111) Nanomesh. *Phys. Chem. Chem. Phys.* **2014**, *16*, 12374−12384.
(29) Huang, M.; Yan, H.; Chen, C.; Song, D.; Heinz, T.; Hone, J. Phonon Softening and Crystallographic Orientation of Strained Graphene Studied by Raman Spectroscopy. *Proc. Natl. Acad. Sci. U. S. A.* **2009**, *106*, 7304−7308.
(30) Couto, N. J. G.; Costanzo, D.; Engels, S.; Ki, D.-K.; Watanabe, K.; Taniguchi, T.; Stampfer, C.; Guinea, F.; Morpurgo, A. F. Random Strain Fluctuations as Dominant Disorder Source for High-Quality On-Substrate Graphene Devices. *Phys. Rev. X* **2014**, *4*, 041019.
(31) Sutter, P. W.; Flege, J.-I.; Sutter, E. A. Epitaxial Graphene on Ruthenium. *Nat. Mater.* **2008**, *7*, 406−411.
(32) Man, K. L.; Altman, M. S. Low Energy Electron Microscopy and Photoemission Electron Microscopy Investigation of Graphene. *J. Phys: Condens. Matt.* **2012**, *24*, 314209.
(33) Mende, P.; Gao, Q.; Ismach, A.; Chou, H.; Widom, M.; Ruoff, R.; Colombo, L.; Feenstra, R. Characterization of Hexagonal Boron Nitride Layers on Nickel Surfaces by Low-Energy Electron Microscopy. *Surf. Sci.* **2017**, *659*, 31−42.
(34) Petrovic, M.; Hagemann, U.; Horn-von Hoegen, M.; zu Heringdorf, F.-J. M. Microanalysis of Single-Layer Hexagonal Boron Nitride Islands on Ir(111). *Appl. Surf. Sci.* **2017**, *420*, 504−510.
(35) Felter, J.; Raths, M.; Franke, M.; Kumpf, C. *In Situ* Study of Two-Dimensional Dendritic Growth of Hexagonal Boron Nitride. *2D Mater.* **2019**, *6*, 045005.
(36) Man, K. L.; Altman, M. S. Small-Angle Lattice Rotations in Graphene on Ru(0001). *Phys. Rev. B: Condens. Matter Mater. Phys.* **2011**, *84*, 235415.
(37) Hemmi, A.; Bernard, C.; Cun, H. Y.; Roth, S.; Klöckner, M.; Kälin, T.; Weinl, M.; Gsell, S.; Schreck, M.; Osterwalder, J.; Greber, T. High Quality Single Atomic Layer Deposition of Hexagonal Boron Nitride on Single Crystalline Rh(111) Four-Inch Wafers. *Rev. Sci. Instrum.* **2014**, *85*, 035101.
(38) Greber, T.; Raetzo, O.; Kreutz, T. J.; Schwaller, P.; Deichmann, W.; Wetli, E.; Osterwalder, J. A Photoelectron Spectrometer for K-Space Mapping above the Fermi Level. *Rev. Sci. Instrum.* **1997**, *68*, 4549−4554.
(39) Ma, H.; Brugger, T.; Berner, S.; Ding, Y.; Iannuzzi, M.; Hutter, J.; Osterwalder, J.; Greber, T. Nano-Ice on Boron Nitride Nanomesh: Accessing Proton Disorder. *ChemPhysChem* **2010**, *11*, 399−403.
(40) Altman, M. S. Trends in Low Energy Electron Microscopy. *J. Phys.: Condens. Matter* **2010**, *22*, 084017.
(41) Bauer, E. *Surface Microscopy with Low Energy Electrons*; Springer: New York, 2014.
(42) Yu, K. M.; Lau, K. L. W.; Altman, M. S. Fourier Optics of Image Formation in Aberration-Corrected LEEM. *Ultramicroscopy* **2019**, *200*, 160−168.

https://dx.doi.org/10.1021/acsnano.0c08616
ACS Nano XXXX, XXX, XXX−XXX

(43) Hutter, J.; Iannuzzi, M.; Schiffmann, F.; VandeVondele, J. Cp2k: Atomistic Simulations of Condensed Matter Systems. *Wiley Interdiscip. Rev.: Comput. Mol. Sci.* **2014**, *4*, 15−25.
(44) Perdew, J. P.; Burke, K.; Ernzerhof, M. Generalized Gradient Approximation Made Simple. *Phys. Rev. Lett.* **1996**, *77*, 3865−3868.
(45) Vydrov, O. A.; Van Voorhis, T. Nonlocal van der Waals Density Functional Made Simple. *Phys. Rev. Lett.* **2009**, *103*, 63004−63007.
(46) Sabatini, R.; Gorni, T.; de Gironcoli, S. Nonlocal van der Waals Density Functional Made Simple and Efficient. *Phys. Rev. B: Condens. Matter Mater. Phys.* **2013**, *87*, 41108−41111.
(47) Goedecker, S.; Teter, M.; Hutter, J. Separable Dual-Space Gaussian Pseudopotentials. *Phys. Rev. B: Condens. Matter Mater. Phys.* **1996**, *54*, 1703−1710.
(48) VandeVondele, J.; Hutter, J. Gaussian Basis Sets for Accurate Calculations on Molecular Systems in Gas and Condensed Phases. *J. Chem. Phys.* **2007**, *127*, 114105.

https://dx.doi.org/10.1021/acsnano.0c08616
ACS Nano XXXX, XXX, XXX−XXX